ACS APPLIED ELECTRONIC MATERIALS

Open Access
This article is licensed under CC-BY 4.0

Long-Persistent Photoconductivity in Transistor Structures Made from Thin ZrS_3-Films

Lars Thole,* Asem Ben Kalefa, Christopher Belke, Sonja Locmelis, Lina Bockhorn, Peter Behrens, and Rolf J. Haug

Cite This: ACS Appl. Electron. Mater. 2023, 5, 6286−6291

Read Online

ACCESS | Metrics & More | Article Recommendations

ABSTRACT: In the search for two-dimensional (2D) materials, transition-metal trichalcogenides (TMTCs) have emerged as promising candidates for optoelectronic applications. Here, we show a very long-lasting persistent photoconductivity (PPC) over several hours in thin films of the TMTC zirconium trisulfide (ZrS_3) at room temperature when illuminated with a 470 nm LED. ZrS_3 crystals were grown using chemical vapor transport. UV−vis spectroscopy showed an indirect band gap of 1.81 eV and an Urbach energy of 83 meV, indicating that the system has a large number of defects. Transistor measurements on thin layers with thicknesses varying between 19 and 50 nm showed ZrS_3 to be an n-type semiconductor. The conductivity increases under illumination, and it only reaches the original state several hours after switching off the illumination. This PPC can be described by using a stretched exponential function. On top of that, the sum of three exponential functions with tree different relaxation times fits the observed PPC nearly equally well. This shows that three processes dominate the relaxation. The three observed processes can be differentiated with respect to their origin by their dependence on the thickness of the thin layers.

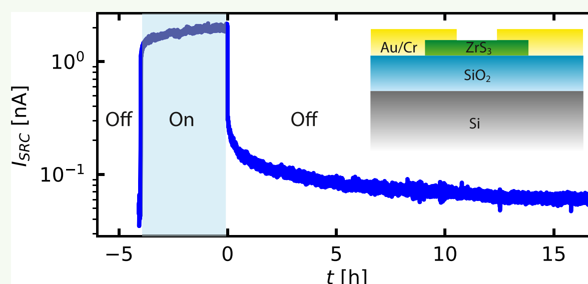

KEYWORDS: *2D materials, transition-metal trichalcogenides, ZrS_3, persistent photoconductivity, chemical vapor transport, Urbach energy, field effect, defects*

Downloaded via 89.245.22.250 on April 9, 2024 at 09:08:13 (UTC).
See https://pubs.acs.org/sharingguidelines for options on how to legitimately share published articles.

INTRODUCTION

Since the discovery of graphene, there has been a huge interest in two-dimensional materials.[1−3] As graphene lacks a band gap, a significant part of research lies in finding two-dimensional semiconductors for electronic and optoelectronic applications.[4] Recently, there has been a focus on transition-metal chalcogenides of the form MX_a, where M is a transition metal, X is a chalcogen, and a is the stoichiometric factor. Most commonly known is the group of transition-metal dichalcogenides (TMDC) of the form MX_2 and its most prevalent material MoS_2.[5,6] There are, however, several more promising materials. One of these materials is zirconium trisulfide (ZrS_3), of the transition-metal trichalcogenides (TMTC), which have the form MX_3. TMTCs as a material class show new unique properties, such as the significant anisotropy within a layer.[7,8] ZrS_3 crystals, as well as nanobelts in particular, have shown a high photoresponse, especially under blue and ultraviolet light.[9−11] Nanostructures also showed an anisotropic response to light owing to their crystal structure.[12] ZrS_3 consists of several layers held together by a van der Waals force. This opens up the possibility for devices made from thin layers. Figure 1a shows the crystal structure of ZrS_3 illustrated using Vesta.[13] In each of the layers, the Zr atoms are forming one-dimensional chains, which are separated by S atoms, leading to a big anisotropy within a layer.

In this article, we are presenting measurements on bulk and, in particular, on thin-layered ZrS_3. UV−vis spectroscopy is used to determine the band gaps of the bulk material. Additionally, the material shows a significant Urbach energy, which is an indicator for disorder in the crystal.[14] Our investigations of the photoconductivity in thin layers of ZrS_3 reveal an extraordinarily long persistent photoconductivity (PPC) over several hours stemming from defects in the material.

RESULTS AND DISCUSSION

ZrS_3 crystals as grown can be seen in Figure 1b as a scanning electron microscopy (SEM) image. The anisotropy of the crystal structure leads to a growth of needle-like structures of few mm size. On this bulk crystal, UV−vis spectroscopy was

Received: August 23, 2023
Revised: September 21, 2023
Accepted: October 9, 2023
Published: October 24, 2023

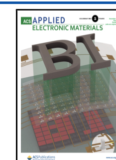

© 2023 The Authors. Published by American Chemical Society

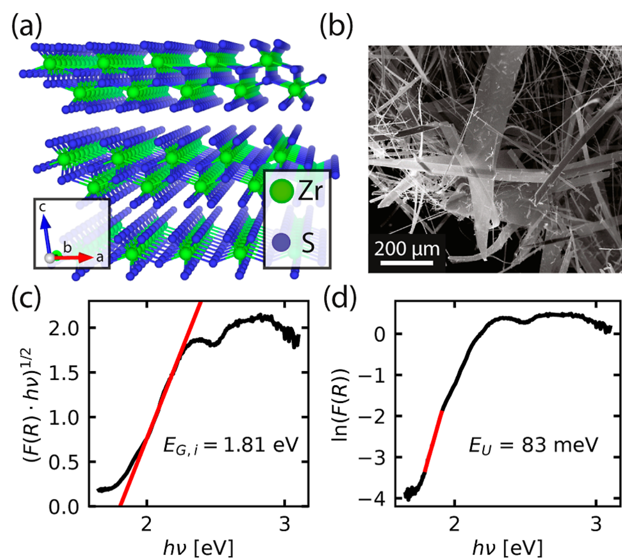

Figure 1. (a) Crystal structure of ZrS_3. The layers are held together by van der Waals force. (b) SEM-picture of bulk ZrS_3. (c) Tauc plot for the UV−vis spectroscopy data of ZrS_3, showing an indirect band gap of 1.81 eV. (d) Logarithmic presentation of the spectroscopy data. The linear part gives an Urbach energy of 83 meV.

carried out to determine the band gap of ZrS_3. Here, the reflectance R of the material was measured, and the Kubelka−Munk function

$$F(R) = \frac{(1 - R)^2}{2R} \tag{1}$$

was used to estimate the absorption of the materials.[15,16] The Tauc plot is shown in Figure 1c.

An indirect band gap energy of E_G = 1.81 eV can be determined[17] by using a linear fit, as seen in Figure 1c, and the relation

$$(F(R)\cdot h\nu)^{1/2} \propto h\nu - E_G \tag{2}$$

with the Planck constant h and the frequency of the photon ν. Figure 1c shows this indirect transition, where the data is plotted with an exponent of 1/2 on the y-axis.[18] The corresponding direct band gap can be determined as 2.33 eV by changing the exponent of the plotted data from 1/2 to 2. This value is close to the recently reported 2 eV for the direct band gap,[19] however lower than the reported value of 2.8 eV from 1973.[20]

In addition to the band gap excitation, the absorption spectrum shows an exponential increase for lower energies just below the indirect band gap, called the Urbach tail.[14,21−23] Here we get the exponential relation

$$F(R) \propto \exp(h\nu/E_U) \tag{3}$$

with E_U being the Urbach energy. The slope of a linear fit through the logarithm of $F(R)$ in that area, as seen in Figure 1d, gives a value of 83 meV for the Urbach energy E_U. This Urbach energy is a signature of an appreciable disorder in this semiconductor, likely caused by sulfur vacancies seen in EDX measurements, where the material shows a stoichiometry of $ZrS_{2.96}$. Sulfur vacancies have been found and investigated in TMDCs.[24−28]

To create thin films of ZrS_3, the bulk material was exfoliated using the standard Scotch-tape-method. Thereby, several samples of different thicknesses were produced. One of the samples was transferred onto hexagonal boron nitride (hBN) to decrease the influence from the substrate in field effect measurements. Contacts were designed by using e-beam lithography. For photoconductivity measurements, a blue LED with a wavelength of 470 nm (intensity ≈ 40 mW/cm^2) was used.

Figure 2 shows field effect measurements on a thin flake of 34 nm which was transferred onto an hBN layer with a thickness d_{hBN} = 21 nm seen in the inset.

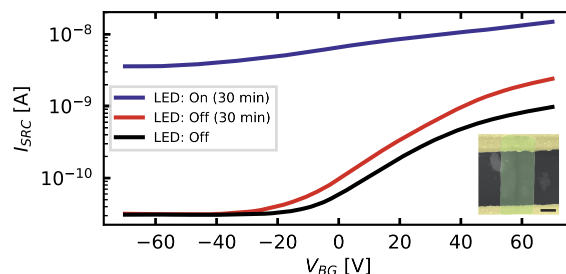

Figure 2. Field effect in thin ZrS_3 transferred onto hBN under the influence of light. The black curve shows the original current for the sample in the dark. The blue curve shows the current after the sample was illuminated for 30 min. After the light was turned off, there was still conductivity left coming from the PPC. The red curve shows the current 30 min after the light was turned off. The inset shows the used sample (green) in contact with Cr/Au contacts (yellow) as an atomic force microscope image. The scale bar corresponds to 1 μm.

Here, heavily doped silicon functions as the backgate, while SiO_2 with a thickness d_{SiO_2} = 340 nm and the hBN function as the dielectric layer. The black curve shows the measurement for the sample without illumination, where the backgate was varied from −70 to 70 V. The current was measured for a constant voltage of V_{SRC} = 5 V. The increasing current with gate voltage is typical for n-type semiconductors. From the linear part of the curve between 40 and 60 V, a mobility μ = 0.5 × 10^{-3} $cm^2/(V\ s)$ can be extracted using

$$\mu = \frac{dI_{SRC}}{dV_{BG}} \cdot \frac{L}{WV_{SRC}C} \tag{4}$$

where, L = 3.5 μm is the length between contacts, W = 2.5 μm is the width, and C = 9.3 × 10^{-5} F m^{-2} is the capacitive coupling calculated by

$$C = \frac{\epsilon_0 \epsilon_{r,SiO_2} \epsilon_{r,hBN}}{(d_{SiO_2}\epsilon_{r,hBN} + d_{hBN}\epsilon_{r,SiO_2})} \tag{5}$$

with $\epsilon_{r,hBN}$ = 3.76 and ϵ_{r,SiO_2} = 3.9. The mobility in the sample is low when compared to other 2D materials such as MoS_2,[5] which can be attributed to a high amount of defects. The curve shows an on/off ratio of about 3 × 10^2. The blue curve shows a measurement under illumination with a 470 nm LED after the sample was already illuminated for 30 min. Here, we can observe a clear increase in current by 1 order of magnitude in the on-state and two in the off-state in comparison to the dark state. The mobility also increases to 3.6 × 10^{-3} $cm^2/(V\ s)$, while the on/off ratio decreases to 2 × 10^1. After the light is turned off, it is still possible to see an increased current compared to the dark state and an increased mobility of 1.45 × 10^{-3} $cm^2/(V\ s)$, as seen for the red curve in Figure 2. This is attributed to a persistent photoconductivity effect.

https://doi.org/10.1021/acsaelm.3c01163
ACS Appl. Electron. Mater. 2023, 5, 6286−6291

To study the PPC in more detail, we analyzed the time dependence of the current shown in Figure 3a for a sample with a thickness of 45 nm not transferred onto hBN.

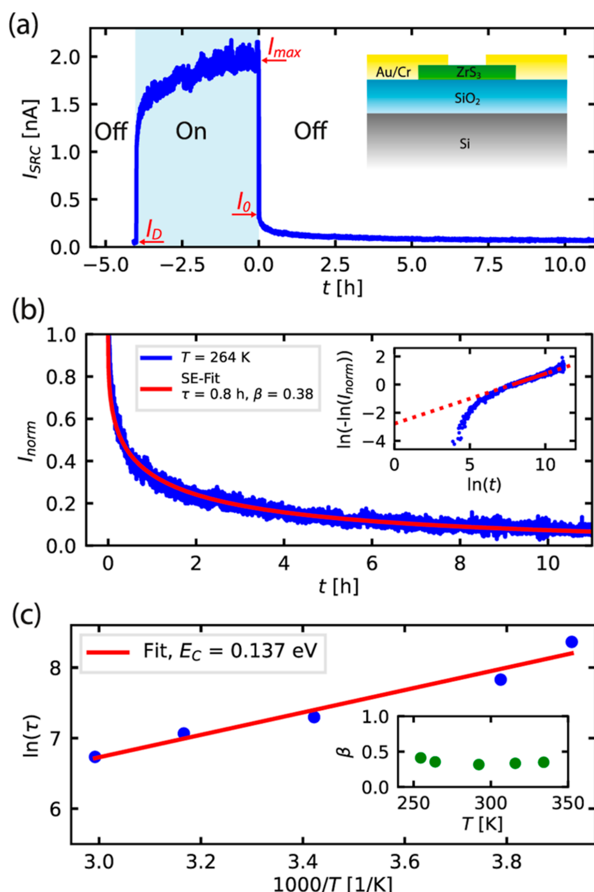

Figure 3. (a) Persistent photoconductivity seen in ZrS_3 at 264 K. The current starts in a dark state I_D for a voltage of 4 V, then after a blue LED is turned on rises to a maximum current I_{max}. After the LED is turned off, there is an instant recombination of carriers. Afterward, a slow decay in current is visible, starting at I_0. The inset shows the sample structure. (b) PPC normalized to I_0 with a SE fit. The inset shows the data plotted with logarithms, enabling a linear fit. (c) Decay constant τ in an Arrhenius plot.

Here, we observe the expected immediate increase of the current when the LED is turned on and an astonishingly slow further increase in the current. When the light is turned off, the current immediately drops to a point I_0 because of instantly recombining charge carriers. Afterward, we observe a decay over several hours until the current goes back to the dark state I_D, showing an extremely long PPC effect even at room temperature.

For further investigation, we normalize the current to get the current I_{norm} by using the relation

$$I_{norm} = \frac{I_{SRC} - I_D}{I_0 - I_D} \quad (6)$$

which features the source current I_{SRC}, the dark current I_D, and the starting current I_0. In this representation, shown in Figure 3b, the PPC can be seen clearly. Here, a decay over a period of more than 10 hours is visible. For disordered samples with a range of different relaxation processes, this decay in the current I_{PPC} is typically described by using a stretched exponential (SE) function

$$I_{PPC} = \exp(-t/\tau)^{\beta} \quad (7)$$

with a characteristic time constant τ and a stretching exponent β.[29−32] The red curve in Figure 3b shows the fitted SE function. In the inset of Figure 3b, the data are plotted logarithmically, where τ and β can be extracted by using a linear fit. Here, the PPC is described as originating from captured carriers. These carriers have to overcome an energy barrier E_C, which leads to a long-lasting current I_{PPC}. This means the PPC should get slower with a lower temperature T. This is seen in the time constant τ, which depends on the capture barrier E_C by

$$\tau = \tau_0 \exp\left(\frac{E_C}{k_b T}\right) \quad (8)$$

where k_b is the Boltzmann constant. To obtain E_C, we can use measurements at different temperatures and plot the resulting time constant τ in an Arrhenius plot where $\ln(\tau)$ is plotted against $1000/T$, as shown in Figure 3c. Here, a linear fit is used to extract a capture energy E_C of 0.137 eV. The inset in Figure 3c shows that there is only a small change of β with the temperature for the varying time constants τ.

The PPC was observed in many other semiconductor materials, where it is often only in a range of a few seconds at about room temperature.[33−42] A high longevity of the PPC at room temperature has been seen in a few TMDCs, such as MoS_2.[43−51]

In order to identify the relaxation processes leading to the SE fit, we used a fit with different decay processes. Assuming three different processes, we were successful in obtaining nearly perfect fits. The fit function for three different processes is of the form

$$I_{PPC} = k_1 \cdot \exp(-t/\tau_1) + k_2 \cdot \exp(-t/\tau_2) + k_3 \cdot \exp(-t/\tau_3) \quad (9)$$

where the amplitude gives the contribution of each process and sums up to 1 which means

$$\Sigma_i k_i = 1 \quad (10)$$

and each k_i represents one decay process. Figure 4a,b shows the triple exponential fit compared to the SE fit for temperatures of 334 and 255 K, respectively.

The involved processes are characterized by the individual time constants τ_i, which vary quite drastically, τ_1 is on the order of several hours, τ_2 is on the order of an hour, and τ_3 in an order of only a few minutes. For a temperature of 334 K, τ_1 is 4.5 h, τ_2 is 0.5 h, and τ_3 is 1.5 min, whereas for a temperature of 255 K, τ_1 is 18.6 h, τ_2 is 2 h, and τ_3 is 9.1 min. A capture energy can be attributed to each of these processes by using an Arrhenius plot of the time constants τ_i, as shown in Figure 4c. This leads to quite similar capture energies for τ_1 and τ_2 with 0.1 and 0.11 eV, respectively. The shortest time constant, τ_3 leads to a slightly higher capture energy of 0.16 eV.

Looking at samples with different thicknesses gives an idea of the origins of these processes. The thickness dependence of each k is shown in Figure 5a for three samples with thicknesses of 19, 37, and 50 nm.

Here, we observe a clear trend for k_2 to increase with increasing thickness while both k_1 and k_3 decrease. This means

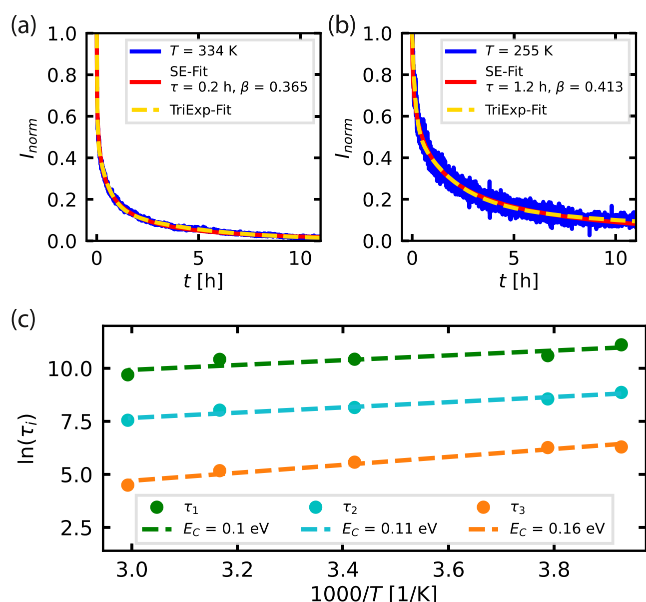

Figure 4. PPC with SE fit and the corresponding triple exponential function for temperatures of (a) 334 and (b) 255 K. Since the data can be fitted well by the triple exponential function, we can assume there are three processes involved in the PPC. (c) Arrhenius-plot for the individual τ_i. With a linear fit, a capture energy E_C can be extracted. This gives the energy barrier that each of the involved processes has.

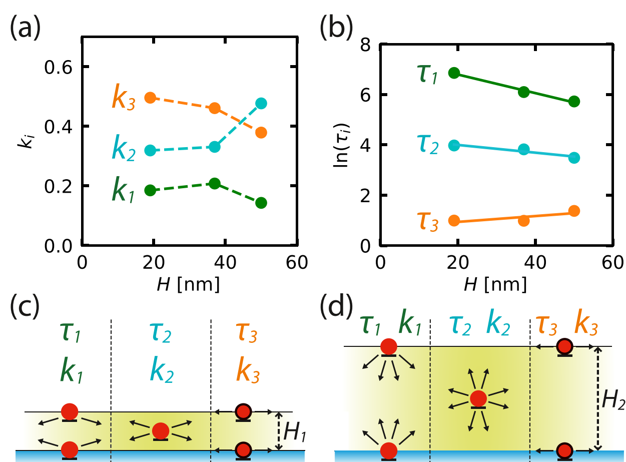

Figure 5. Thickness dependence of (a) k_i and (b) τ_i showing the change in contribution for each process. Schematic of the recombination processes in (c) a thin sample with a thickness of H_1 and (d) a thick sample with a thickness of H_2, with H_1¡H_2. For τ_1 and τ_3, the defect is in the surface or interface of the sample. For τ_2, the defect is inside the material. In the case of τ_1 and τ_2, the trapped charge carriers have more options to recombine in the bulk material for thicker samples, while for τ_3, they recombine on the surface or interface independently of the thickness.

that for thicker, more bulk-like samples, the process behind k_2 becomes more dominant. This can be attributed to a decay process that is based on effects found in the bulk material. The decreases in k_1 and k_3 for thicker samples indicate that the corresponding decay processes stem from defects on the surface or interface to the substrate.

Figure 5b shows the change in the different τ_i values for samples with different thicknesses. Here, τ_1 and τ_2 show a decreasing behavior, while τ_3 shows a slight increase for increasing thickness. As τ_3 is the fastest of the relaxation times and any deviation is comparatively big compared to the absolute value, it is difficult to gauge the exact nature of this process. The decrease of τ_1 and τ_2 with a higher thickness can be attributed to more phase space for the recombination process in a more bulk-like structure compared to a more two-dimensional structure. In the case of thinner ZrS_3, the recombination process becomes more confined, leading to longer relaxation times.

As the contribution of k_2 increases with a higher thickness and, at the same time, τ_2 decreases, we can clearly see the cause to be a bulk process, such as the sulfur vacancies detected in the EDX measurements and with the high Urbach energy. For k_1, which is decreasing at the same time, it can be assumed that it is a process caused by defects on the surface or interface of the sample. The clearly decreasing τ_1 shows that the recombination process happens in the bulk of the sample, which could be caused by chemical defects on the surface of the sample. This gets more evident when looking at the very similar capture energies E_C of 0.1 and 0.11 eV for τ_1 and τ_2. These two processes have a similar source, most likely the known sulfur vacancies, with the difference being one in the bulk and one on the interface or surface of the sample. The shortest process k_3 shows a clear decrease for thicker samples, meaning it is located at the surface or interface of the sample. Since the corresponding τ_3 is staying more or less constant and only slightly increasing for thicker samples, the recombination process does not become faster in a more bulk-like structure. This is a clear sign that the process is caused by defects on the interface, which can be attributed to foreign atoms or molecules, such as water molecules introduced during the sample preparation process, as found for several other 2D materials.[52] The underlying scattering processes as described are schematically shown in Figure 5c for a thin sample and in Figure 5d for a thick sample.

■ CONCLUSIONS

The material ZrS_3 was synthesized by chemical transport, exfoliated onto a SiO_2/Si substrate, and contacted by e-beam lithography. The bulk material shows an indirect band gap of 1.81 eV and an Urbach energy of 83 meV, indicating a significant amount of defects in the material. Transistor measurements on thin layers were done, showing that the material is an n-type semiconductor. Illuminating the sample showed a significant increase in conductance. Further, the current after illumination shows a PPC that persists over a long time of several hours. It was possible to use a SE function to fit the decay, also showing a capture energy of 0.137 eV. However, a fit with a combination of three exponential functions could be used equally well to fit the decaying current. This shows that the PPC in this material originates from three different processes. By investigating the thickness dependence of these processes, the PPC can be attributed to defects in the bulk and at the interface, which can be distinguished clearly. The bulk process relaxes faster for thicker films due to the increase in phase space, meaning that thin films show an extraordinary long PPC effect.

■ METHODS

Sample Preparation. A chemical transport method was used for the synthesis of bulk ZrS_3. Powdered elements in a molar ratio of S/Zr = 3/1 with an excess of sulfur (5% mass) to avoid impurity phases such as ZrS_2 are used for synthesis. The purities of Zr and S were 99.6

https://doi.org/10.1021/acsaelm.3c01163
ACS Appl. Electron. Mater. 2023, 5, 6286−6291

and 99.99%, respectively. The precursor materials were sealed in an evacuated quartz ampule (length 150 mm, diameter 10 mm) together with 5 mg of iodine per cm^3. Afterward, it was sintered at 650 °C for 7 days. The ampule is then placed in a two-part oven with temperatures of 650 °C on one side and 600 °C on the other side for 21 days. This temperature gradient leads to the formation of crystals on the cooler side. Several sublimations back and forth are carried out in the ampule to improve the homogeneity of the material. An average composition of $ZrS_{2.96}$ was determined by SEM−EDX analysis (Hitachi Regulus 8230, EDX: Oxford Ultimax 100). The XRD data were collected at room temperature on a Stadi P Stoe powder diffractometer with Cu $K_{\alpha 1}$ radiation in the range $5° < 2\theta < 80°$. The material adopts the $P2_1/m$ structure, and the lattice parameters are in good agreement with previously reported data with a = 511,51(19) pm, b = 378,04(16) pm, c = 911,38(169) pm, and β = 97,409(55)°.[53]

Thin films of ZrS_3 were exfoliated from the bulk material onto a substrate of highly doped silicon with a 340 nm silicon dioxide layer using the standard Scotch-tape-method. For electrical measurements, contacts were designed using e-beam lithography, where Cr and Au were evaporated on the sample to produce electrical contacts. Thickness was determined by using an atomic force microscope.

Measurement Methods. All of the measurements were performed as two-terminal DC measurements with Keithley 2400 measurement devices. For field effect measurements, silicon was used as a backgate. The measurements are done under vacuum with a Peltier element to control the temperature in the measurement system. For photoconductivity measurements, a blue LED with a wavelength of 470 nm was used.

AUTHOR INFORMATION

Corresponding Author

Lars Thole − *Institut für Festkörperphysik, Leibniz Universität Hannover, 30167 Hannover, Germany*; orcid.org/0000-0002-6468-6289; Email: thole@nano.uni-hannover.de

Authors

Asem Ben Kalefa − *Institut für Festkörperphysik, Leibniz Universität Hannover, 30167 Hannover, Germany*

Christopher Belke − *Institut für Festkörperphysik, Leibniz Universität Hannover, 30167 Hannover, Germany*

Sonja Locmelis − *Institut für Anorganische Chemie, Leibniz Universität Hannover, 30167 Hannover, Germany*

Lina Bockhorn − *Institut für Festkörperphysik, Leibniz Universität Hannover, 30167 Hannover, Germany*

[‖]**Peter Behrens** − *Institut für Anorganische Chemie and Laboratorium für Nano- und Quantenengineering, Leibniz Universität Hannover, 30167 Hannover, Germany*

Rolf J. Haug − *Institut für Festkörperphysik, Leibniz Universität Hannover, 30167 Hannover, Germany; Laboratorium für Nano- und Quantenengineering, Leibniz Universität Hannover, 30167 Hannover, Germany*

Complete contact information is available at: https://pubs.acs.org/10.1021/acsaelm.3c01163

Notes

The authors declare no competing financial interest.

[‖]Passed away on the 13th of January 2023.

ACKNOWLEDGMENTS

This work was funded by the Deutsche Forschungsgemeinschaft (DFG, German Research Foundation) under Germany's Excellence Strategy-EXC 2123 Quantum Frontiers-390837967 and EXC 2122 PhoenixD-390833453 and within the Priority Program SPP 2244 '2DMP'.

REFERENCES

(1) Novoselov, K. S.; Geim, A. K.; Morozov, S. V.; Jiang, D.; Zhang, Y.; Dubonos, S. V.; Grigorieva, I. V.; Firsov, A. A. Electric Field Effect in Atomically Thin Carbon Films. *Science* **2004**, *306*, 666−669.

(2) Geim, A. K.; Grigorieva, I. V. Van der Waals heterostructures. *Nature* **2013**, *499*, 419−425.

(3) Novoselov, K. S.; Mishchenko, A.; Carvalho, A.; Castro Neto, A. H. 2D materials and van der Waals heterostructures. *Science* **2016**, *353*, aac9439.

(4) Castellanos-Gomez, A. Why all the fuss about 2D semiconductors? *Nat. Photonics* **2016**, *10*, 202−204.

(5) Radisavljevic, B.; Radenovic, A.; Brivio, J.; Giacometti, V.; Kis, A. Single-layer MoS_2 transistors. *Nat. Nanotechnol.* **2011**, *6*, 147−150.

(6) Mak, K. F.; Lee, C.; Hone, J.; Shan, J.; Heinz, T. F. Atomically thin MoS_2: A new direct-gap semiconductor. *Phys. Rev. Lett.* **2010**, *105*, 136805.

(7) Island, J. O.; Molina-Mendoza, A. J.; Barawi, M.; Biele, R.; Flores, E.; Clamagirand, J. M.; Ares, J. R.; Sánchez, C.; Van Der Zant, H. S.; D'Agosta, R.; Ferrer, I. J.; Castellanos-Gomez, A. Electronics and optoelectronics of quasi-1D layered transition metal trichalcogenides. *2D Mater.* **2017**, *4*, 022003.

(8) Chen, M.; Li, L.; Xu, M.; Li, W.; Zheng, L.; Wang, X. Quasi-One-Dimensional van der Waals Transition Metal Trichalcogenides. *Research* **2023**, *6*, 0066.

(9) Patel, A.; Patel, K.; Limberkar, C.; Patel, K. D.; Solanki, G. K.; Pathak, V. M. Wavelength dependent anisotropic photosensing activity of zirconium trisulfide crystal. *J. Mater. Sci.: Mater. Electron.* **2022**, *33*, 8417−8425.

(10) Tao, Y. R.; Wu, X. C.; Xiong, W. W. Flexible Visible-Light Photodetectors with Broad Photoresponse Based on ZrS_3 Nanobelt Films. *Small* **2014**, *10*, 4905−4911.

(11) Tao, Y. R.; Wu, J. J.; Wu, X. C. Enhanced ultraviolet-visible light responses of phototransistors based on single and a few ZrS_3 nanobelts. *Nanoscale* **2015**, *7*, 14292−14298.

(12) Wang, X.; Wu, K.; Blei, M.; Wang, Y.; Pan, L.; Zhao, K.; Shan, C.; Lei, M.; Cui, Y.; Chen, B.; Wright, D.; Hu, W.; Tongay, S.; Wei, Z. Highly Polarized Photoelectrical Response in vdW ZrS_3 Nanoribbons. *Adv. Electron. Mater.* **2019**, *5*, 1900419.

(13) Momma, K.; Izumi, F. VESTA 3 for three-dimensional visualization of crystal, volumetric and morphology data. *J. Appl. Crystallogr.* **2011**, *44*, 1272−1276.

(14) Ayik, C.; Studenyak, I.; Kranjec, M.; Kurik, M. Urbach Rule in Solid State Physics. *Int. J. Opt. Appl.* **2014**, *4*, 76−83.

(15) Ferrer, I. J.; Ares, J. R.; Clamagirand, J. M.; Barawi, M.; Sánchez, C. Optical properties of titanium trisulphide (TiS_3) thin films. *Thin Solid Films* **2013**, *535*, 398−401.

(16) Makuła, P.; Pacia, M.; Macyk, W. How To Correctly Determine the Band Gap Energy of Modified Semiconductor Photocatalysts Based on UV-Vis Spectra. *J. Phys. Chem. Lett.* **2018**, *9*, 6814−6817.

(17) Belke, C. Untersuchung von Dünnschicht-Übergangsmetall-Chalkogeniden hinsichtlich ihrer elektrischen Eigenschaften. Doctoral dissertation, Leibniz University Hannover, Germany, 2021.

(18) Tauc, J.; Grigorovici, R.; Vancu, A. Optical Properties and Electronic Structure of Amorphous Germanium. *Phys. Status Solidi B* **1966**, *15*, 627−637.

(19) Flores, E.; Ares, J. R.; Ferrer, I. J.; Sánchez, C. Synthesis and characterization of a family of layered trichalcogenides for assisted hydrogen photogeneration. *Phys. Status Solidi RRL* **2016**, *10*, 802−806.

(20) Schairer, W.; Shafer, M. W. Growth and optical absorption spectra of the layer-type trichalcogenides ZrS_3 and HfS_3. *Phys. Status Solidi A* **1973**, *17*, 181−184.

(21) Urbach, F. The Long-Wavelength Edge of Photographic Sensitivity and of the Electronic Absorption of Solids. *Phys. Rev.* **1953**, *92*, 1324.

(22) Hassanien, A. S.; Akl, A. A. Effect of Se addition on optical and electrical properties of chalcogenide CdSSe thin films. *Superlattices Microstruct.* **2016**, *89*, 153−169.

(23) Ikhmayies, S. J.; Ahmad-Bitar, R. N. A study of the optical bandgap energy and Urbach tail of spray-deposited CdS:In thin films. *J. Mater. Res. Technol.* **2013**, *2*, 221−227.
(24) Le, D.; Rawal, T. B.; Rahman, T. S. Single-layer MoS_2 with sulfur vacancies: Structure and catalytic application. *J. Phys. Chem. C* **2014**, *118*, 5346−5351.
(25) Li, L.; Qin, Z.; Ries, L.; Hong, S.; Michel, T.; Yang, J.; Salameh, C.; Bechelany, M.; Miele, P.; Kaplan, D.; Chhowalla, M.; Voiry, D. Role of sulfur vacancies and undercoordinated Mo regions in MoS_2 nanosheets toward the evolution of hydrogen. *ACS Nano* **2019**, *13*, 6824−6834.
(26) Gali, S. M.; Pershin, A.; Lherbier, A.; Charlier, J. C.; Beljonne, D. Electronic and Transport Properties in Defective MoS_2: Impact of Sulfur Vacancies. *J. Phys. Chem. C* **2020**, *124*, 15076−15084.
(27) Liang, Q.; Zhang, Q.; Zhao, X.; Liu, M.; Wee, A. T. S. Defect engineering of two-dimensional transition-metal dichalcogenides: Applications, challenges, and opportunities. *ACS Nano* **2021**, *15*, 2165−2181.
(28) Bretscher, H.; Li, Z.; Xiao, J.; Qiu, D. Y.; Refaely-Abramson, S.; Alexander-Webber, J. A.; Tanoh, A.; Fan, Y.; Delport, G.; Williams, C. A.; Stranks, S. D.; Hofmann, S.; Neaton, J. B.; Louie, S. G.; Rao, A. Rational Passivation of Sulfur Vacancy Defects in Two-Dimensional Transition Metal Dichalcogenides. *ACS Nano* **2021**, *15*, 8780−8789.
(29) Lysenko, V. S.; Gomeniuk, Y. V.; Kondratenko, S. V.; Melnichuk, Y. Y.; Kozyrev, Y. N.; Teichert, C. Transport and Photoelectric Effects in Structures with Ge and SiGe Nanoclusters Grown on Oxidized Si (001). *Adv. Mater. Res.* **2013**, *854*, 11−19.
(30) Lee, M.; Lee, W.; Choi, S.; Jo, J.-W.; Kim, J.; Park, S. K.; Kim, Y.-H.; Lee, M.; Lee, W.; Choi, S.; Kim, Y.-h.; Jo, J.-w.; Park, S. K.; Kim, J. Brain-Inspired Photonic Neuromorphic Devices using Photodynamic Amorphous Oxide Semiconductors and their Persistent Photoconductivity. *Adv. Mater.* **2017**, *29*, 1700951.
(31) Li, J. Z.; Lin, J. Y.; Jiang, H. X.; Geisz, J. F.; Kurtz, S. R. Persistent photoconductivity in $Ga_{1-x}In_xNyAs_{1-y}$. *Appl. Phys. Lett.* **1999**, *75*, 1899−1901.
(32) Wu, N.; Wang, C.; Slattum, P. M.; Zhang, Y.; Yang, X.; Zang, L. Persistent Photoconductivity in Perylene Diimide Nanofiber Materials. *ACS Energy Lett.* **2016**, *1*, 906−912.
(33) Queisser, H. J.; Theodorou, D. E. Decay kinetics of persistent photoconductivity in semiconductors. *Phys. Rev. B: Condens. Matter Mater. Phys.* **1986**, *33*, 4027−4033.
(34) Jiang, J.; Wen, Y.; Wang, H.; Yin, L.; Cheng, R.; Liu, C.; Feng, L.; He, J. Recent Advances in 2D Materials for Photodetectors. *Adv. Electron. Mater.* **2021**, *7*, 2001125.
(35) Lang, D. V.; Logan, R. A.; Jaros, M. Trapping characteristics and a donor-complex (DX) model for the persistent-photoconductivity trapping center in Te-doped $Al_xGa_{1-x}As$. *Phys. Rev. B: Condens. Matter Mater. Phys.* **1979**, *19*, 1015−1030.
(36) Nelson, R. J. Long-lifetime photoconductivity effect in n-type GaAlAs. *Appl. Phys. Lett.* **1977**, *31*, 351−353.
(37) Mooney, P. M. Deep donor levels (DX centers) in III-V semiconductors. *J. Appl. Phys.* **1990**, *67*, R1−R26.
(38) Tarun, M. C.; Selim, F. A.; McCluskey, M. D. Persistent photoconductivity in strontium titanate. *Phys. Rev. Lett.* **2013**, *111*, 187403.
(39) Hirsch, M. T.; Wolk, J. A.; Walukiewicz, W.; Haller, E. E. Persistent photoconductivity in n-type GaN. *Appl. Phys. Lett.* **1997**, *71*, 1098−1100.
(40) Lang, D. V.; Logan, R. A. Large-lattice-relaxation model for persistent photoconductivity in compound semiconductors. *Phys. Rev. Lett.* **1977**, *39*, 635−639.
(41) Buscema, M.; Island, J. O.; Groenendijk, D. J.; Blanter, S. I.; Steele, G. A.; Van Der Zant, H. S.; Castellanos-Gomez, A. Photocurrent generation with two-dimensional van der Waals semiconductors. *Chem. Soc. Rev.* **2015**, *44*, 3691−3718.
(42) Katz, O.; Garber, V.; Meyler, B.; Bahir, G.; Salzman, J. Gain mechanism in GaN Schottky ultraviolet detectors. *Appl. Phys. Lett.* **2001**, *79*, 1417−1419.
(43) George, A.; Fistul, M. V.; Gruenewald, M.; Kaiser, D.; Lehnert, T.; Mupparapu, R.; Neumann, C.; Hübner, U.; Schaal, M.; Masurkar, N.; Arava, L. M.; Staude, I.; Kaiser, U.; Fritz, T.; Turchanin, A. Giant persistent photoconductivity in monolayer MoS_2 field-effect transistors. *npj 2D Mater. Appl.* **2021**, *5* (1), 15−18.
(44) Rathi, N.; Rathi, S.; Lee, I.; Wang, J.; Kang, M.; Lim, D.; Khan, M. A.; Lee, Y.; Kim, G. H. Reduction of persistent photoconductivity in a few-layer MoS_2 field-effect transistor by graphene oxide functionalization. *RSC Adv.* **2016**, *6*, 23961−23967.
(45) Wu, Y. C.; Liu, C. H.; Chen, S. Y.; Shih, F. Y.; Ho, P. H.; Chen, C. W.; Liang, C. T.; Wang, W. H. Extrinsic Origin of Persistent Photoconductivity in Monolayer MoS_2 Field Effect Transistors. *Sci. Rep.* **2015**, *5*, 11472−11510.
(46) Li, X.; Lin, M. W.; Puretzky, A. A.; Basile, L.; Wang, K.; Idrobo, J. C.; Rouleau, C. M.; Geohegan, D. B.; Xiao, K. Persistent photoconductivity in two-dimensional $Mo_{1-x}W_xSe_2$-$MoSe_2$ van der Waals heterojunctions. *J. Mater. Res.* **2016**, *31*, 923−930.
(47) Zhang, K.; Peng, M.; Yu, A.; Fan, Y.; Zhai, J.; Wang, Z. L. A substrate-enhanced MoS_2 photodetector through a dual-photogating effect. *Mater. Horiz.* **2019**, *6*, 826−833.
(48) Furchi, M. M.; Polyushkin, D. K.; Pospischil, A.; Mueller, T. Mechanisms of photoconductivity in atomically thin MoS_2. *Nano Lett.* **2014**, *14*, 6165−6170.
(49) Di Bartolomeo, A.; Genovese, L.; Foller, T.; Giubileo, F.; Luongo, G.; Croin, L.; Liang, S. J.; Ang, L. K.; Schleberger, M. Electrical transport and persistent photoconductivity in monolayer MoS_2 phototransistors. *Nanotechnology* **2017**, *28*, 214002.
(50) Cho, K.; Kim, T. Y.; Park, W.; Park, J.; Kim, D.; Jang, J.; Jeong, H.; Hong, S.; Lee, T. Gate-bias stress-dependent photoconductive characteristics of multi-layer MoS_2 field-effect transistors. *Nanotechnology* **2014**, *25*, 155201.
(51) Chandan; Sarkar, S.; Angadi, B. Defects induced persistent photoconductivity in monolayer MoS_2. *Appl. Phys. Lett.* **2021**, *118*, 172105.
(52) Peng, Z.; Yang, R.; Kim, M. A.; Li, L.; Liu, H. Influence of O_2, H_2O and airborne hydrocarbons on the properties of selected 2D materials. *RSC Adv.* **2017**, *7*, 27048−27057.
(53) Furuseth, S.; Brattås, L.; Kjekshus, A.; Andresen, A. F.; Fischer, P. On the Crystal Structures of TiS_3, ZrS_3, $ZrSe_3$, $ZrTe_3$, HfS_3, and $HfSe_3$. *Acta Chem. Scand., Ser. A* **1975**, *29*, 623−631.

https://doi.org/10.1021/acsaelm.3c01163
ACS Appl. Electron. Mater. 2023, 5, 6286−6291